IOPscience iopscience.iop.org

Home Search Collections Journals About Contact us My IOPscience

Solid-state reaction of nickel silicide and germanide contacts to semiconductor nanochannels

This content has been downloaded from IOPscience. Please scroll down to see the full text.

2014 Semicond. Sci. Technol. 29 054004

(http://iopscience.iop.org/0268-1242/29/5/054004)

View the table of contents for this issue, or go to the journal homepage for more

Download details:

IP Address: 137.110.192.10
This content was downloaded on 02/04/2014 at 17:33

Please note that terms and conditions apply.

IOP Publishing
Semiconductor Science and Technology
Semicond. Sci. Technol. 29 (2014) 054004 (18pp)
doi:10.1088/0268-1242/29/5/054004

Solid-state reaction of nickel silicide and germanide contacts to semiconductor nanochannels

Wei Tang[1,2], Binh-Minh Nguyen[2,3], Renjie Chen[3] and Shadi A Dayeh[3]

[1] Department of Materials Science and Engineering, University of California, Los Angeles, CA 90024, USA
[2] Center for Integrated Nanotechnologies, Los Alamos National Laboratory, Los Alamos, NM 87545, USA
[3] Department of Electrical and Computer Engineering, University of California, San Diego, CA 92093, USA

E-mail: sdayeh@eng.ucsd.edu

Received 1 November 2013, revised 27 January 2014
Accepted for publication 11 February 2014
Published 1 April 2014

Abstract
The surge in advancing the materials science of solid-state reactions for nanoscale contacts to advanced semiconductor devices necessitates a comprehensive dissemination and discussion on recent progress. The objective of this work is to review the notable developments in compound and alloy contact formation to nanoscale nanowire channels made of germanium, silicon, and their heterostructures, and to develop a unifying framework for understanding the significantly distinct reaction behaviors from those commonly observed in bulk. The Ni-based compound and alloy contacts are used as a platform to highlight the size-relevant, thermodynamic, and kinetic differences, and their key material, reaction, and electronic parameters and properties are summarized. Special attention is given to the interplay between the compound/alloy contact structure and the resultant electronic properties.

Keywords: nanowire, contact, silicide, germanide, *in situ* TEM

(Some figures may appear in colour only in the online journal)

1. Introduction

The metal–semiconductor contact properties play a critical role in every solid-state device used for electronic applications. Notable examples of devices whose performance is significantly influenced by the contact properties include solar cells, power devices, and state-of-the-art field effect transistors (FETs). Some of the most sophisticated work in the area of metal–semiconductor contacts is fueled by the need to meet enhanced performance demands in transistor scaling. As the transistor channel length shrinks below 20 nm in the most advanced technology node, reliable and low resistance contacts are demanded more than ever in order to fully realize the performance of ultra-scaled devices. For traditional Si devices, the silicide contact technology has experienced a transition from $TiSi_2$, to $CoSi_2$ and to the current NiSi technology in order to meet the requirements of low resistance, low thermal budget and good thermal stability [1, 2]. For emerging high mobility Ge/Si_xGe_{1-x} p-type metal–oxide–semiconductor (PMOS) and III–V n-type MOS (NMOS) channel [3], similar compound/alloy contacts like metal germanide, germano-silicide and metal/III–V are being actively investigated. On the other hand, 3D nanoscale transistor channel (referred as nanochannel henceforth) device geometries including nanowires (NWs) and FinFETs present new opportunities for contact studies; in these devices, the contact formation process has proven to be different from planar devices. This work serves to provide a comprehensive review of the recent understandings for the formation process of Ni-based contacts to Si, Ge, and Si/Ge core/shell NWs, and to present an in-depth treatment of their kinetic, thermodynamic, and size-relevant behaviors. The interrelated structure/electronic

© 2014 IOP Publishing Ltd Printed in the UK

Table 1. Summary of structural and electrical properties of various Ni silicide phases. Source: [1].

Phases	Lattice	a (Å)	b (Å)	c (Å)	Density (g cm^{-3})	V per Si Atom (Å^3)	Resistivity ($\mu\Omega$ cm)
$Ni_{31}Si_{12}$	Hexagonal	6.671	–	1.228	7.56	39.6	90–150
δ-Ni_2Si*	Orthorhombic	4.99	3.72	7.06	7.37	32.8	24–30
θ-Ni_2Si*	Hexagonal	3.836	–	4.948	7.88	30.7	–
NiSi	Orthorhombic	5.175	3.332	5.609	5.97	24.1	10–18
$NiSi_2$	Cubic	5.416	–	–	4.80	19.7	34–50
Si	Cubic	5.430	–	–	2.33	19.9	–

*δ-Ni_2Si and θ-Ni_2Si structural data are from [12].

property aspects are emphasized, the overall influence on FET device properties is summarized and remaining issues are discussed.

2. Ni–Si solid-state reaction and their contacts to NWFETs

2.1. Ni silicide formation in Si nanochannels

The prevailing application of Ni silicide as a contact to Si-based transistor devices continues to arouse active fundamental materials science studies of the Ni–Si binary system. In thin film planar reactions (i.e. Ni films reacting with bulk Si), it is well known that the formed Ni silicide phase during the reaction between Ni and Si is largely determined by the reaction temperature. As the temperature is increased, δ-Ni_2Si is the first phase that forms above 200 °C, which then transforms to NiSi for temperatures above 350 °C, and finally converts to $NiSi_2$ at temperatures above 750 °C [1, 2, 4].

In Si nanochannels, the Ni–Si diffusional reaction follows a different phase sequence. The most typical reaction geometry is that of a Si NW contacted with top Ni pads, which act as reservoirs for providing Ni during silicide formation, and as electrical contacts to the Si NW. Controlling the leading phase in Ni silicide formation is important from a device perspective because the leading Ni silicide phase that is in direct contact with the Si NW determines the Schottky barrier height (SBH) for charge injection/extraction from the Si NW. In addition, the detailed atomic configuration at the interface determines the strain that is applied to the Si channel after silicide formation, which potentially alters the carrier mobilities. Figure 1(*a*) shows a transmission electron microscope (TEM) image of a typical phase formation sequence for Ni silicide [5] when the Ni pad reacts with the Si NW at a reaction temperature of 400 °C. The $NiSi_2$ is the leading phase, followed by θ-Ni_2Si, δ-Ni_2Si and $Ni_{31}Si_{12}$. This phase sequence can be generally reproduced at a broader temperature range (300–650 °C) [6–8] with minor differences (presence/absence) in some of the Ni-rich intermediate phases. NiSi is generally missing in the Si NW silicidation phase sequence, except for some special treatments, such as point contact reactions [9, 10] or with Pt insertion [8]. The results in Ni silicide formation in NWs contrast their bulk counterpart, in which only NiSi forms in the temperature range of 375–750 °C. This distinction opens up new opportunities to understand the silicide phase formation mechanism in general non-planar geometries for current and next generation transistors [3].

During the Ni silicide formation in Si NWs, the selection of the leading phase is independent of the NW growth direction. Figure 1(*b*) and (*c*) shows that $NiSi_2$ emerges as the leading phase in both ⟨1 1 1⟩ and ⟨1 1 2⟩ oriented Si NWs. This is in contrast to a previous study [11] showing the θ-Ni_2Si as the leading phase in ⟨1 1 2⟩ grown NWs.

Except for $NiSi_2$, other Ni silicide phase segments, including θ-Ni_2Si, δ-Ni_2Si and $Ni_{31}Si_{12}$, experience volume expansion after silicide conversion and their volume per Si atom is compared in table 1. In addition to the radial volume relaxation represented by expansion of the NW diameter, it is important to investigate if there exists a simultaneous volume relaxation along the axial direction of the NW. To address this question, we calculated the theoretical volume expansion of each of the Ni silicide phases, assuming only radial expansion, and compared these values with those obtained from the experimentally observed cross-sectional area expansion for the same silicide segment. The former is the ratio of the volume per Si atom in different silicides to that in the Si crystal, and the latter is directly derived from TEM images from four different NWs, and the results are shown in figure 1(*e*). The θ-Ni_2Si is the first silicide phase showing volume expansion. The experimentally measured cross-sectional expansion of θ-Ni_2Si segment is smaller than that expected from the theoretical volume expansion (lower than the 45° line), which suggests that axial volume relaxation occurs along with the NW radial expansion, and the Si atoms may have to back diffuse against the incoming Ni flux. The δ-Ni_2Si and $Ni_{31}Si_{12}$ data are spread across both sides of the theoretical curve. This spread implies that their radial expansion also relies on the difference between the amount of back-diffused Si atoms received from the previous phase and those passed to the next phase.

Volume expansion is an inherent characteristic in NW silicide formation, and by constraining the volume expansion, the silicide growth behavior can be tailored. Several groups have reported retarded growth rate when Ni silicides grow into Si NWs with SiO_x [6, 13] and Al_2O_3 [8] coatings. The Ni diffusivity is believed to be lowered with compressive strain exerted by the SiO_x shells on the Si NWs. This can potentially be beneficial from an electrical resistivity perspective because high Ni content silicides such as $Ni_{31}Si_{12}$ that demand large volume expansion would be prohibited to grow. Since $Ni_{31}Si_{12}$ is characterized by the largest resistivity among other silicides, constraining the Si NW channel with an oxide shell can therefore lead to the reduction of parasitic series resistances.

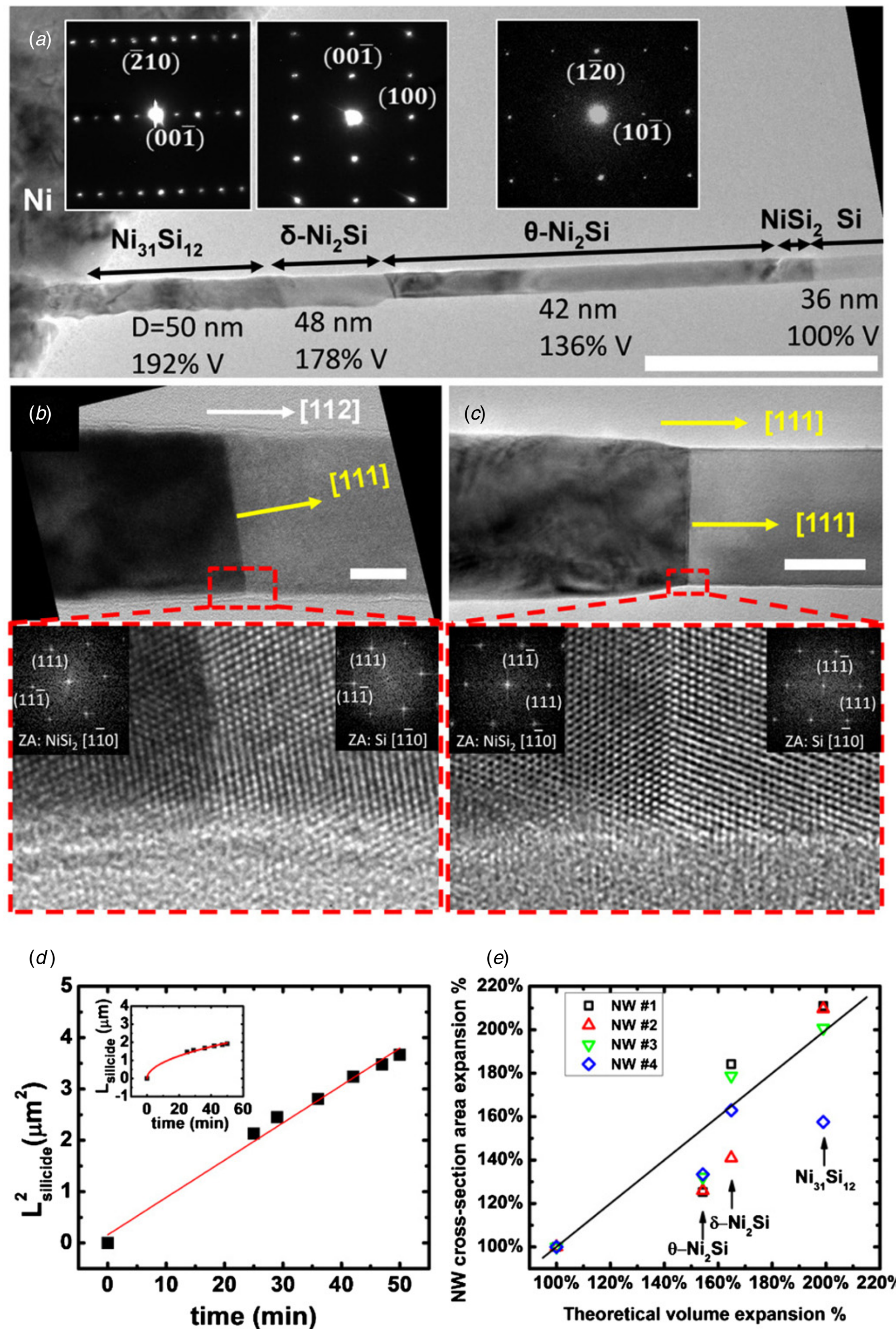

Figure 1. (*a*) TEM image showing nickel silicide phase sequence: between Ni and Si, several phases are formed including $Ni_{31}Si_{12}$, δ-Ni_2Si,θ-Ni_2Si and $NiSi_2$. Zone axes for inset diffraction patterns from left to right are (1 2 0), (0 1 0), and (2 1 2), respectively. The scale bar is 400 nm. (*b*) and (*c*) TEM image of the $NiSi_2/Si$ interface, showing the reaction front is Si (1 1 1) plane in both ⟨1 1 2⟩ and ⟨1 1 1⟩ oriented silicon NWs. The scale bars are 20 nm and 50 nm respectively (*d*) Growth kinetics curve of Ni–Si NW reaction at 400 °C, showing typical diffusion limited parabolic time dependence. (*e*) The expansion of the NW cross-sectional area of Ni silicide segments with different phases versus the theoretical volume expansion. Reproduced with permission from [5].

There are several major differences in the Ni–Si reaction between bulk Si and Si NWs. *Firstly*, in the Ni reaction with Si NWs, the Ni source (Ni pad) is abundant compared with the Si source (Si NW), whereas the Si supply is essentially unlimited in a typical thin film planar reaction. This represents two extremes of relative abundance of the binary solid-state reactants, and different thermodynamic treatments should be considered to understand the corresponding reactions. In the Si-rich regime, nickel silicides generally react with Si until the complete formation of the thermodynamically most stable

Table 2. Enthalpy of formation for nickel silicides reacting with excess Si (thin film planar reaction). The thermodynamic data are adapted from the recommended values in [14].

Reaction	ΔH_f (kJ mol^{-1})	ΔH_f (kJ cm^{-3})	Molar volume (cm^3)
$2Ni + Si = Ni_2Si$	−141	−7.08	19.9
$3Ni_2Si + Si = 2Ni_3Si_2$	−15	−0.43	34.4
$Ni_3Si_2 + Si = 3NiSi$	−11	−0.75	14.6
$Ni_2Si + Si = 2NiSi$	−16	−1.09	14.6
$NiSi + Si = NiSi_2$	−2	−0.07	23.6

Table 3. Enthalpy of formation for nickel silicides reacting with excess Ni and limited Si (Si NW case). Thermodynamic data are based on the recommended values in [1, 14].

Reaction	ΔH_f (kJ mol^{-1})	ΔH_f (kJ cm^{-3})	Molar volume (cm^3)
$2Si + Ni = NiSi_2$	−88	−3.72	23.6
$NiSi_2 + Ni = 2NiSi$	−42	−2.90	14.6
$NiSi + Ni = Ni_2Si$	−55	−2.74	19.9
$NiSi_2 + 3Ni = 2Ni_2Si$	−97	−4.87	19.9
$12Ni_2Si + 7Ni = Ni_{31}Si_{12}$	−1819	−6.39	284.7

phase, the $NiSi_2$ phase. The relevant reactions in the Si rich regime (thin film planar reaction), including their enthalpy of formation, are compiled in table 2.

The driving force for a reaction is determined from the total reduction of the Gibbs energy:

$$\Delta G_f = \Delta H_f - T\Delta S_f \tag{1}$$

where ΔG_f, ΔH_f and ΔS_f are the energy, enthalpy and entropy of formation at temperature T. Usually, the term $T\Delta S_f$ is negligibly small in solid-state reactions such that $\Delta H_f \approx \Delta G_f$ [15]. Conventionally, $NiSi_2$ formation is perceived as nucleation controlled, which can only occur at temperatures above 800 °C. The reason behind this perception is that the ΔH_f driving force for the reaction $NiSi + Si = NiSi_2$ is only −0.07 kJ cm^{-3}, so the nucleation barrier is high. We note that the above situation of small driving force is only true in the planar thin film reaction, where $NiSi_2$ forms after NiSi formation with high temperatures.

In the reaction with Si NWs, the sustained Ni and limited Si supplies drives the resulting silicides into Ni-rich phases. For the case of excess Ni and limited Si, the reactions and their corresponding enthalpy of formation are listed in table 3.

It is noted that ΔH_f of the reaction $Ni + 2Si = NiSi_2$ is −3.72 kJ cm^{-3} which is larger in magnitude compared to those of NiSi and Ni_2Si, so the high formation energy for $NiSi_2$ in this direct Ni–Si reaction can suppress the $NiSi_2$ nucleation barrier. This suppression results in the low-temperature (⩽400 °C) formation of $NiSi_2$ as the first phase in a Ni vapor to Si reaction [16] and in oxide mediated epitaxy [17]. In the NW reaction, various groups [5–7, 11, 13] have reported $NiSi_2$ formation as the leading phase at low temperatures. These observations do not contradict with the existing interpretations from Ni reaction with planar films in the Ni-rich situation. In addition to $NiSi_2$, the driving forces for other more Ni-rich silicides are generally also large in this Ni excess regime. This suggests that the nucleation is not the limiting step in determining the leading phase [18] and corroborates with the fact that multiple Ni silicide phases grow simultaneously during the reaction between Ni and Si NWs. In fact, it has been experimentally demonstrated by TEM that multiple silicide phases simultaneously nucleate at the very beginning of the reaction with Si NWs [7] or with thin Si planar films [19]. The fundamental mechanisms of first phase selection in binary system reaction have been intensively investigated, from both thermodynamic and kinetic aspects. Theories focusing on thermodynamic origins include the lowest temperature eutectic model [20] and the effective heat of formation model [15]. On the other hand, kinetic competitive growth models suggest that the first phase is the one that grows the fastest [21]. In such context, the nucleation is not attributed as the rate limiting step, because forming any nickel silicide phase directly from Ni and Si would provide a sufficient driving force to overcome the nucleation barrier [18]. A comprehensive review of the theories about first phase formation can be found in [19]. The kinetic origin may explain why $NiSi_2$ forms as the leading phase in a NW reaction. Another possible mechanism will be discussed in the next section.

Secondly, the Ni diffusion mechanism may be potentially different in the reaction of Ni with Si NWs. Appenzeller *et al* were the first to discuss different Ni diffusion mechanisms such as surface versus volume diffusion in the nickel silicide formation in Si NWs [22]. The relationship between silicide growth length $L_{Silicide}$ and NW radius R was plotted in the form of $L_{Silicide}$ versus R^{-1} and R^{-2}. It was concluded that the Ni volume diffusion is the dominant diffusion mechanism, because only the fitting line of $L_{Silicide}$ versus R^{-2} was found to pass through the origin point where $L_{silicide}$ should approach zero for infinitely large NW ($R^{-2} \approx 0$) at short silicide growth times. The underlying assumption is that the amount of diffused Ni (measured by the volume of converted Ni silicide segment $L_{silicide} \cdot R^2$) should be constant among different NW diameters. Katsman *et al* argued that the volume diffusion mechanism cannot explain the very fast growth rate of nickel silicide at a low temperature (280 °C) in [22], and a Ni surface diffusion mechanism is proposed to account for the fast growth rate. Dellas *et al* [23] and Chen *et al* [7] investigated the temperature-dependent Ni silicide growth in Si NWs at high temperature regimes. To better understand the difference of the Ni silicide diffusional growth in NWs, we compile the results from all these efforts, including ours, together with the vast amount of reports on Ni reaction with thin films, (reviewed in [24]) in a single Arrhenius plot in figure 2. The kinetic parameter to consider is the growth constant κ, which is defined in the following well-known relationship in the diffusional growth:

$$L^2_{silicide}(t) - L^2_{silicide}(0) = \kappa t. \tag{2}$$

From figure 2, we can extract a variety of important information.

(1) From the reports on reaction of Ni with bulk Si, the growth constant of various Ni silicides fall relatively in a band, indicated by dashed lines in figure 2, and can be different

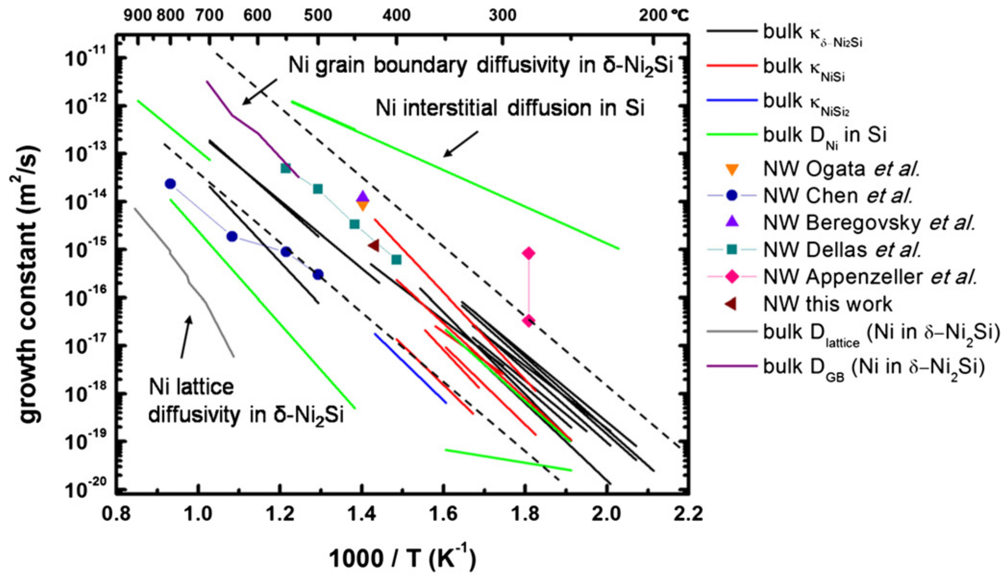

Figure 2. Arrhenius plot of Ni silicide formation in Si NWs and bulk counterparts. Data for studies on Si NWs are adapted from Ogata *et al* [13], Chen *et al* [7], Beregovsky *et al* [25], Dellas *et al* [23], Appenzeller *et al* [22]. Data from studies on bulk Si are adapted from [24] and [26].

by a factor of ~500 at a given temperature depending on the details of the samples and the Ni silicide phases that form.

(2) The majority of the NW results fall within the band, suggesting that the $NiSi_2$ leading phase does not significantly alter the growth constant compared with that of the bulk case. Given the fact that the majority of the Ni silicide extension into the NW is δ-Ni_2Si and θ-Ni_2Si, the comparison to the bulk δ-Ni_2Si data is more relevant. Although bulk diffusion data for θ-Ni_2Si is not available, we assume that it has a comparable diffusivity to δ-Ni_2Si as Ni atoms form continuous sub-lattices in both structures [27].

(3) The bulk D_{lattice} (lattice diffusivity) of Ni in Ni_2Si is much lower (out of the band) than the κ in both NW and bulk cases, which implies that other more efficient diffusion mechanisms should be present to assist the Ni silicide growth. The grain boundary (GB) diffusion is usually attributed as the dominant diffusion mechanism in the bulk Ni_2Si growth, since D_{GB} falls in the band in figure 2 and shows a closer activation energy (1.71 eV) to the reported $\kappa_{\delta-Ni_2Si}$ ranging from 1.3 to 1.8 eV. However, in the reaction between Ni and the Si NW, the GBs along the NW direction are usually absent and surface diffusion was proposed by multiple authors [13, 23, 28] as the dominant diffusion mechanism. As noted by these authors, the surface diffusion is actually diffusion along the interface between Ni silicide and the native oxide pre-existing on the surface of the Si NW. The absence of GB diffusion is ascribed as the reason for formation of $NiSi_2$ as the leading phase, because growth of diffusion controlled phases such as NiSi and Ni_2Si are suppressed. However, the basis of the reasoning above relies on the sole report [29] that decoupled Ni lattice and GB diffusivity in Ni_2Si. In thin film reaction, a huge Ni-to-Si ratio difference (3%) across the Ni_2Si layer was found by RBS measurement after annealing at 250 °C for 24 h [27]. This suggested that there are possibly abundant Ni vacancies at this low temperature and that the Ni lattice diffusivity might have been underestimated.

(4) The report by Appenzeller *et al* [22] presents a remarkable diameter-dependent growth rate of Ni silicide in Si NWs. For NW diameters between 50 and 100 nm, the growth rate can vary by as much as a factor of 5. Investigating the diameter-dependent growth of silicide can shed light on the rate-limiting mechanism of such a process. Here, we used a similar model from [13, 30] and focus on the diameter-dependent growth. If assuming single phase silicide growth, Ni atoms from the Ni reservoir need to (i) dissolve across the Ni/silicide interface, then (ii) diffuse through the already grown silicide segment, and (iii) eventually convert to new layers of Ni silicides at the growth front.

The rates of transport for Ni atoms in the above three processes, neglecting volume expansion and the non-concentric contact geometry, are:

$$I_1 = k_{\text{dissolve}}(C^{\text{eq}}_{\text{silicide/Ni}} - C_0) \cdot (2\pi \text{RL}_b) \tag{3}$$

$$I_2 = -D_{\text{Ni}} \frac{C_L - C_0}{L_{\text{silicide}}} \cdot A \tag{4}$$

$$I_3 = k_{\text{growth}}(C_L - C^{\text{eq}}_{\text{silicide/Si}}) \cdot \pi R^2 \tag{5}$$

where k_{dissolve}, and k_{growth} are the interface reaction rate constants for Ni dissolution into the silicide and Ni reaction with Si at the reaction front. We denote $C^{\text{eq}}_{\text{silicide/Ni}}$ and $C^{\text{eq}}_{\text{silicide/Si}}$ as the equilibrium Ni concentration in Ni silicide when contacted to Ni and Si respectively, and C_0 and C_L are the actual Ni concentration at the respective interfaces (figure 3). The diffusion cross-sectional area A depends on the diffusion path (πR^2 for volume diffusion or $2\pi R\delta$ for surface diffusion, where δ is the atomic layer height). L_b is the length of the NW

Table 4. Diameter-dependent silicide growth in NWs for different growth regimes according to equations [6] and [7].

Nano-silicide growth regimes	A	I	L
Volume diffusion limited ($D_{Ni}/k_{growth}\to 0$, $D_{Ni}/k_{dissolve}\to 0$)	πR^2	$\propto R^2/L_{silicide}$	$\propto t^{1/2}$(Independent of R)
Surface diffusion limited ($D_{Ni}/k_{growth}\to 0$, $D_{Ni}/k_{dissolve}\to 0$)	$2\pi R$	$\propto R/L_{silicide}$	$\propto (t/R)^{1/2}$
Ni source supply limited ($k_{dissolve}/k_{growth}\to 0$, $k_{dissolve}/D_{Ni}\to 0$)	–	$\propto R$	$\propto R^{-1}t$
Interfacial reaction limited ($k_{growth}/k_{dissolve}\to 0$, $k_{growth}/D_{Ni}\to 0$)	–	$\propto R^2$	$\propto t$(Independent of R)

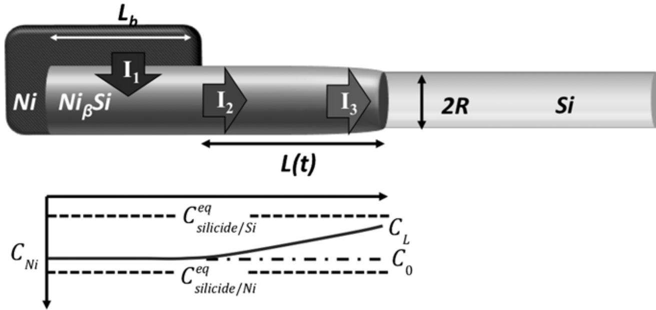

Figure 3. A schematic illustration of Ni silicide growth kinetics.

segment buried under the Ni pad. By solving the steady state condition $I_1 = I_2 = I_3 = I$, I is given by:

$$I = \frac{(C^{eq}_{silicide/Ni} - C^{eq}_{silicide/Si}) \cdot \pi R^2}{\frac{R}{2k_{dissolve}L_b} + \frac{\pi R^2 L_{silicide}(t)}{D_{Ni}A} + \frac{1}{k_{growth}}}. \quad (6)$$

The three terms in the denominator present three rate-limiting mechanisms. The L versus t relationship can be obtained by solving the differential equation

$$\pi R^2 \frac{dL_{silicide}(t)}{dt} = I(t)\frac{M_{Ni_\beta Si}}{N_A \beta \rho_{Ni_\beta Si}} \quad (7)$$

assuming a formed $Ni_\beta Si$ silicide phase, where $M_{Ni_\beta Si}$ is the molar mass of the $Ni_\beta Si$ phase, N_A is Avogadro's number, and $\rho_{Ni_\beta Si}$ is the density of $Ni_\beta Si$ given in table 1. We omit the full solution here but only discuss a few typical regimes and the relevant L, R dependence at a given time (table 4).

The analysis above shows that volume diffusion limited mechanism cannot explain the R-dependent growth length reported in [22]. Katsman *et al* [28] first proposed the $L \propto R^{-1/2}$ dependence for surface diffusion limited silicide growth and was able to fit the data in [22]. The fitting line did not pass through the origin point and the authors argued that the x-axis intercept predicts a critical radius under which a continuous growth front cannot form. However, in order to fully confirm the surface diffusion mechanism, the Ni source supply limited mechanism should be ruled out since it shows a $L \propto R^{-1}$ dependence.

2.2. Role of defects in nanoscale Ni silicide formation

Defects in the NW may contribute significantly to the nucleation and growth of the nickel silicide phase. In advanced semiconductor technology nodes, defects are intentionally built into the device to tailor the stress in the Si channel. The stress memorization technology [31] is one example that utilizes stacking faults to exert tensile strain in the channel by inducing missing planes in the source/drain regions. Understanding the interaction between Ni–Si reaction and defects can be important in controlling the Ni silicide formation in defect-engineered nanochannels. We will first briefly overview how Ni silicide grows in defect free Si NWs, and then compare how defects can change the silicide growth behavior. Using *in situ* transmission electron microscopy (TEM), Chou *et al* demonstrated [10] that Ni silicide grows via a repeating layer-by-layer 2D homogeneous nucleation mechanism (figure 4(*a*)–(*c*)) in a single crystal Si NW. The Si NW/native oxide interface is the only possible heterogeneous site in the system. However, Si/oxide interfaces have low energy and forming a silicide nucleus at such an interface raises the interface energy by creating a high energy silicide/oxide interface. Therefore, heterogeneous nucleation is suppressed and the Ni concentration in the NW continues to increase until it leads to a supersaturation level comparable to or greater than that required for homogeneous nucleation.

The silicide nucleation mechanism has fundamental differences in the presence of defects in Si NWs. By tuning the Si NW growth to different regimes, controlled incorporation of two types of defects can be achieved: (1) twin boundary (TB) along the axial direction of the NW at a high growth pressure regime and (2) nanoscale Si grains deposited at the NW surface at a high growth temperature regime [32]. With the high resolution dynamic imaging capability provided by *in situ* TEM technique, TBs and surface GBs were confirmed as preferred heterogeneous nucleation sites at an atomic scale [33]. Figure 4(*d*) shows one example of a new $NiSi_2$ layer nucleating at the 'corner' site (one of the heterogeneous nucleation sites) and propagating toward the edge of the Si NW. The growth rate is steady (figure 4(*e*)) when the layer-by-layer reaction is guided by repeating heterogeneous nucleation at the center TB.

The effectiveness of nucleation barrier reduction can be evaluated at three different heterogeneous sites (illustrated in figure 5(*b*) inset): (1) TB (2) 'corner', and (3) surface GB, by calculating [33]:

$$\frac{\Delta G^*_{hetero}}{\Delta G^*_{homo}} = \frac{(\pi - \theta) + \sin(\theta)\cos(\theta)}{\pi} \quad (8)$$

where ΔG^*_{hetero} and ΔG^*_{homo} are heterogeneous and homogeneous nucleation barrier respectively. The contact angle θ is given by Young's equation:

$$\bar{\gamma}\cos(\theta) + \gamma_{defect} = \gamma_{new} \quad (9)$$

where $\bar{\gamma}$, γ_{defect} and γ_{new} are different interface energies illustrated in figure 5(*a*). The γ_{defect} and γ_{new} have different meaning and values for different nucleation sites [33]. The $\Delta G^*_{hetero}/\Delta G^*_{homo}$ values are calculated to be 0.93, 0.90, and 0.83, for the nucleation at TBs, 'corners', and the GBs respectively, when choosing reasonable parameters ($\bar{\gamma} = 1.2\gamma^{epi}_{NiSi_2}$).

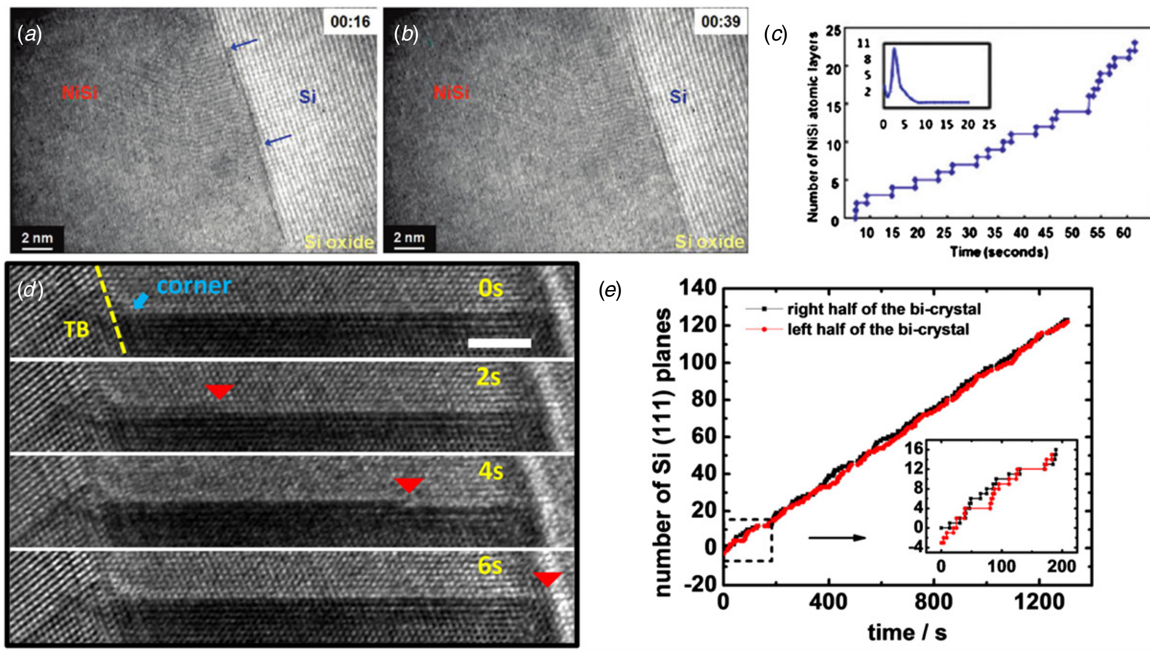

Figure 4. (*a*) and (*b*) homogeneous nucleation of Ni silicide in a single crystal Si NW. (*c*) Layer-by-layer repeating homogeneous nucleation in silicide growth (*d*) $NiSi_2$ heterogeneously nucleates from the 'corner' site. Scale bar is 3 nm. (*e*) The silicide grows at a steady rate when guided by the TB. Inset shows layer-by-layer growth behavior in the heterogeneous nucleation $NiSi_2$ growth. Reproduced with permission from [10, 33].

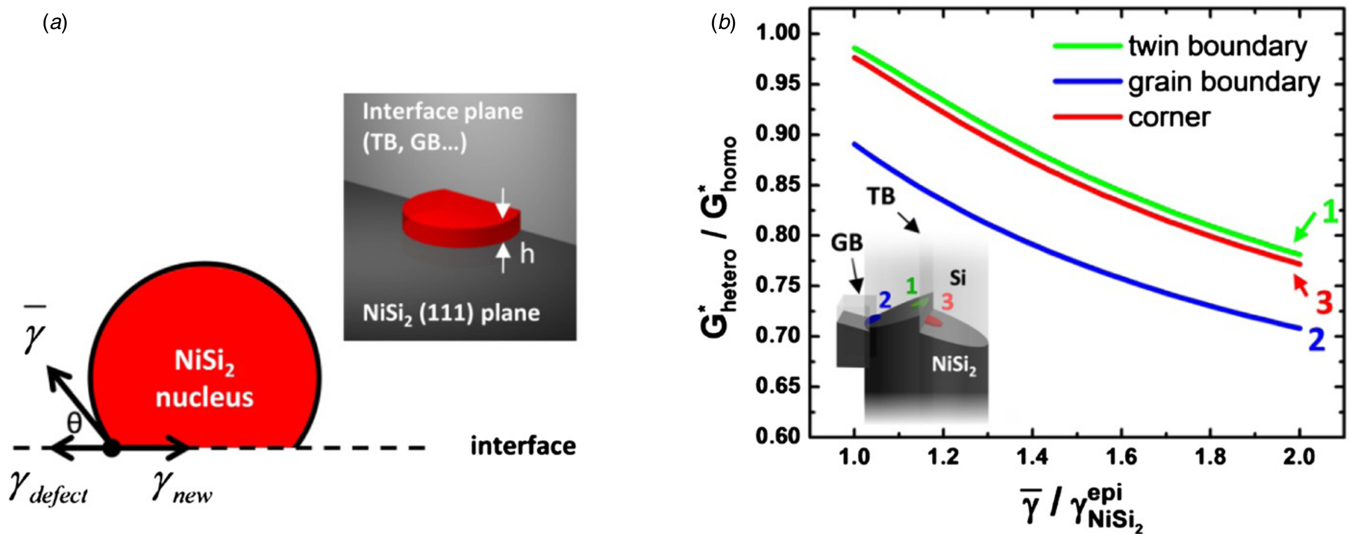

Figure 5. (*a*) Top view of a $NiSi_2$ 2D partial disc heterogeneously nucleated at a certain interface. (*b*) Reduction in the nucleation barrier at different heterogeneous sites noted in the inset schematic which is a 3D view of three different heterogeneous nucleation sites in a defective Si nanowire. Reproduced with permission from [33].

2.3. Ni silicide contact properties and their role in nanoscale devices.

2.3.1. Electronic properties of silicide Schottky barriers. Ni silicides are standard electrical contact materials to Si devices in conventional CMOS technologies. In addition to the low resistance of Ni silicides themselves that allow good current spreading along the width of the device, the magnitude of the SBH between Ni silicides and Si is also important as this determines the contact resistance. The Fermi levels of various Ni silicide phases fall close to the 'mid-gap' of the Si energy band-edge diagram so they can be used as the contact for both NMOS and PMOS devices. Table 5 summarizes the SBH of some Ni silicides and other metal-silicides.

More specifically, Ni silicides have higher electron SBH than that of the hole, but the barrier width can be made sufficiently thin to minimize the contact resistance for both electrons and holes. In addition, the work function of Ni silicides can be adjusted from 4.3 to 5.1 eV by varying the dopant concentration in the Si before silicide formation [35]. The tunability of Ni silicide work function renders it as a widely investigated material as the metal gate contact

Table 5. SBH for electrons of some Ni silicide and other metal-silicide phases.

Silicides	SBH on n-Si (eV) [34]
Ni_2Si	0.75
NiSi	0.75
$NiSi_2$ (type-A, see text)	0.66
$NiSi_2$ (type-B, see text)	0.78
PdSi	0.75
PtSi	0.87
Pt_2Si	0.78
$ErSi_2$	0.39
YSi	0.39

for threshold voltage control [36]. Besides their potential application in devices, epitaxial silicides such as $NiSi_2$ are ideal systems to study fundamental aspects of Schottky barrier (SB) transport. There are two types of coherent $NiSi_2/Si$ interfaces. In a type-A interface, $NiSi_2$ has the same orientation with Si. In a type-B interface, $NiSi_2$ crystal is rotated 180° about the interface normal axis with respect to Si crystal (forming a twin-boundary-like interface). It is known [37] that type-A $NiSi_2/Si$ interface has an electron SBH that is 0.13 eV lower than that of type-B $NiSi_2/Si$ interface. This difference suggests that the interfacial electronic properties and the SBH are determined by the detailed structure of the $NiSi_2/Si$ interface. Apart from Ni silicides, $ErSi_{2-x}$ contacted NMOS [38] and PtSi contacted PMOS [39] NW devices have been demonstrated separately to achieve low SBH for their respective channel carriers.

2.3.2. Ultra-short channel Si NW transistor with Ni silicide source/drain contacts. The reaction between Si and Ni provides the opportunity to define the transistor channel length by a non-lithographic approach. *In situ* TEM provides a unique method to tailor the channel length of a transistor with atomic precision on individual device basis. A three terminal Si NW FET device with 17 nm channel length (figure 6(*b*)) has been demonstrated by controlling the silicidation reaction using this technique [5]. The dynamic reaction process was monitored in real time (figure 6(*a*)) and the growth rate of Ni silicide can be controlled by the annealing temperature.

The ultra-short channel device show higher on-currents than those with longer channel lengths, but its off-state current is higher due to the much larger NW diameter compared with the channel length (figure 6(*c*)) which enforces stronger short channel effects. By investigating the dependence of maximum transconductance, g_m, versus the channel length, L_G, (figure 6(*d*)), it becomes clear that the Ni silicide/silicon SB contact resistance dominates the on-state conduction, and that the performance gain with down-scaled transistor channels starts to saturate. Figure 6(*d*) inset shows an energy band-edge diagram of a Si NW SB field effect transistor (SBFET) in the on-state with a large potential drop across the contact SB and comparatively much smaller effective carrier-driving potential drop along the channel. Although shorter two-terminal Si NW channels down to 2 nm with Ni silicide [9, 40, 41] and Pt silicide based contacts [39] have been realized, the above trend implies that the SB contact engineering is vital to best fulfil the advantages of short channel SB-FETs. This also implies that mobility extraction using the transconductance method from SBFETs at short channel lengths is largely underestimated [5].

3. Ge, and Ge/Si heterostructured nanochannels

Compared to Si NWs, Ge [42], GeSi [43] or heterostructured Ge/Si [44] NWs are attractive alternatives due to the flexibility in strain and bandgap engineering and due to their intrinsically higher hole mobility for PMOS devices. Similar to the case of Si, the NW geometry is ideally suited to investigate the solid-state reaction of Ge-based materials with metal contacts at nanoscales. Prior research on compound contacts in Ge-based nanochannels followed a similar pathway to that in Si NWs. In this section, we will review some particular results that are different from silicide contacts.

3.1. Nickel germanide formation

Similar to the case of Si, Ni is the material of choice for *p*-contact to Ge due to the small SBH, and the ease to form $NiGe_x$ compounds. However, while the silicide interfacing with Si is usually Si rich ($NiSi_2$), the equivalent germanide phase ($NiGe_2$) is known to be inexistent in ordinary conditions [45]. Instead, different germanide phases have been identified at the germanide/germanium interface. Dellas *et al* [46], annealed Ni contact pads over Ge NWs for 2 min at temperatures ranging between 300 and 400 °C and found that the germanide phase is independent of the growth direction, similar to the case of Si [47]. They used selected area electron diffraction (SAED) in TEM to identify the hexagonal lattice constants of polycrystal $NiGe_x$: a = 3.95 Å and c = 5.187 Å. Dellas *et al* noted that their SAED patterns were similar to those of stoichiometric Ni_2Ge, but they also emphasized the crystal structure similarity with that of other phases (Ni_3Ge_2, Ni_5Ge_3, $Ni_{19}Ge_{12}$, $Ni_{17}Ge_{12}$). Further analysis on the effect of Ni vacancies on the SAED patterns led to a conclusion that the phase was likely to be Ni_3Ge_2 (figure 7(*a*)). Tang *et al* [48] however, reported single crystalline orthorhombic Ni_2Ge (a = 5.11 Å, b = 3.83 Å, c = 7.26 Å) as a result of annealing reaction between Ni and supercritical fluid liquid–solid synthesized ⟨1 1 1⟩ Ge NWs (figure 7(*b*)). The annealing step was performed with *in situ* TEM, at temperatures ranging from 400 to 500 °C. The crystallographic epitaxial relationships were shown to be: Ge(0 1 $\bar{1}$)//Ni_2Ge(0 $\bar{1}$ 1) and Ge(1 $\bar{1}$ $\bar{1}$)//Ni_2Ge(1 0 0). Temperature-dependent growth rate measurements enabled an estimation of the activation energy for the Ni_2Ge growth in Ge NWs to be 0.55 ± 0.05 eV/atom. In addition, temperature-dependent transport measurements of the $Ni_2Ge/Ge/Ni_2Ge$ devices suggested a hole SBH of 0.2 eV at the Ni_2Ge/Ge contact. The authors also demonstrated a clear improvement of NWFET performance after annealing at 400 °C for 15 s, which was attributed to a mobility enhancement from less than 10 cm^2 $(V\ s)^{-1}$ to 65 cm^2 $(V\ s)^{-1}$. When annealed at 650 °C, the germanide interface was shown to be Ni_3Ge with similar crystal structure as Ge: face-centered cubic with the lattice constant: a = 5.74 Å, corresponding to ∼1.5% lattice mismatch to Ge (figure 7(*d*)) [49]. Notably, Ni_3Ge

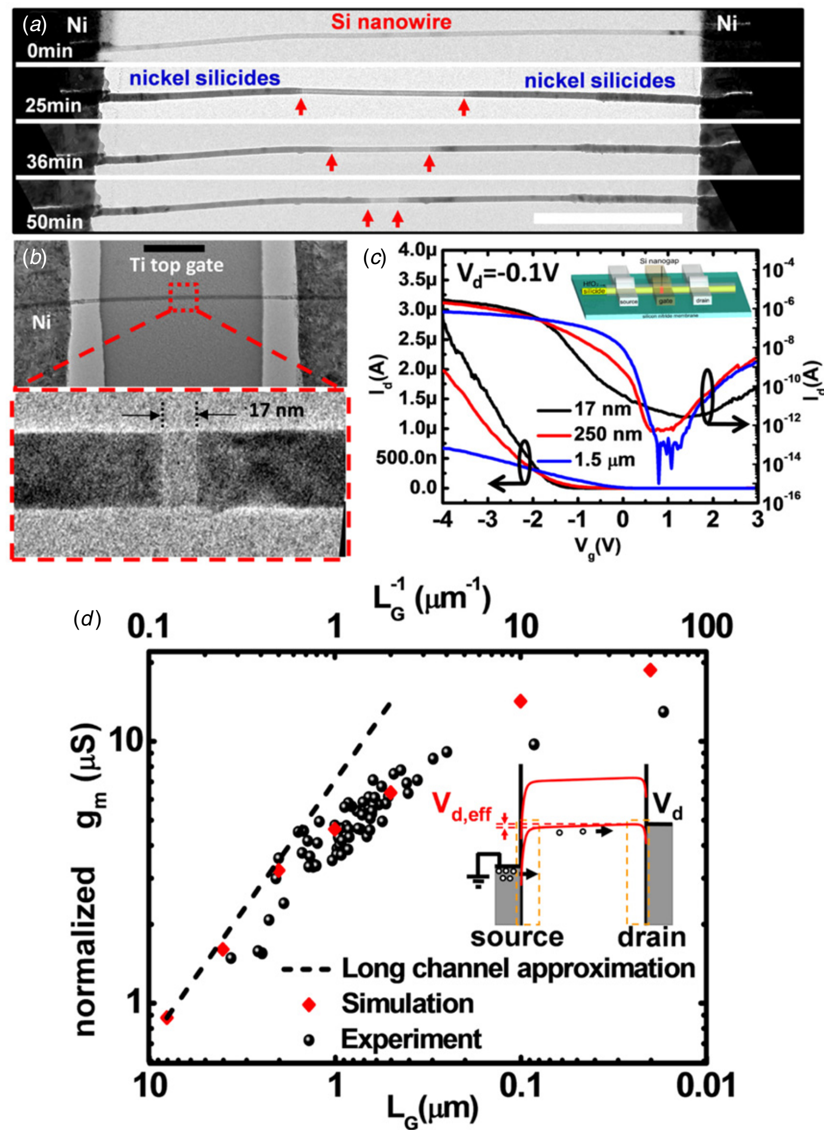

Figure 6. (*a*) Series of *in situ* TEM snapshots showing the growth of nickel silicide from S/D Ni electrodes and narrowing of the middle silicon segment. The red arrows indicate the silicide/silicon reaction front. Scale bar is 1 μm. (*b*) TEM image of a Si NW FET device with 17 nm channel length. Scale bar is 1 μm. (*c*) I_d–V_g characteristics of Si NW FETs with different channel lengths at $V_d = -0.1$V at linear (left *y*-axis) and log (right *y*-axis) scales. Inset is a schematic of the ultra-short channel Si NW FET device (*d*) Channel length-dependent device performance. Inset is the energy band-edge diagram of Si NW SBFET in on-state. Reproduced with permission from [33].

is ferromagnetic at room temperature [50], thus offers great promise for room-temperature spintronic devices. However, the annealing conditions for Ni_3Ge were too harsh for the Ge NWs, which broke due to the high temperature treatment. In fact, the temperature stability appears to be a drawback of Ge NWs in comparison with Si NWs. Broken Ge NWs were also observed by Dellas *et al* [46] in their experiment above 450 °C for unclear reasons. Different possible explanations were proposed, but counter examples were always present, which prevented concluding on a specific hypothesis. Another issue in thermal annealing of Ge NWs is the volume expansion and the segregation of Ni_2Ge nanocrystals on the NW sidewalls, due to the large lattice mismatch between Ge and Ni_2Ge [49].

The germanide interface with Ge NWs can be controlled not only with annealing temperature, but also by radial shell oxide confinement. This is similar to the case of Si NWs where an SiO_x shell was shown to greatly alter the growth rate of different silicide phases [8, 54]. However, in Ge NWs, due to the unstable nature of GeO_x; the phenomenon could not be easily reproduced. In fact, the lack of a high quality, stable oxide in Ge NWs is the reason for strong nanoparticle segregation as discussed above: there is no barrier that blocks Ni diffusion at the surface. Using Al_2O_3 coated by atomic layer deposition, Tang *et al* [51] have shown that a segment of high quality orthorhombic NiGe (a = 5.38 Å, b = 3.42 Å, c = 5.81 Å) was formed between Ni_2Ge and Ge, in contrast to the formation of Ni_2Ge/Ge interfaces as discussed above (figure 7(*c*)). The crystallographic epitaxial relationships at the Ge/NiGe interface were determined to be Ge(01$\bar{1}$)//NiGe(0 1 0) and Ge(1 $\bar{1}$ $\bar{1}$)//NiGe(0 0 1) while those of the NiGe/Ni_2Ge interface were Ni_2Ge(1 0 0)//NiGe(0 1 0) and Ni_2Ge(0 1 1)//NiGe(0 0 1). NiGe segregated particles were only found on the NW/SiO_2 substrate interface, where the

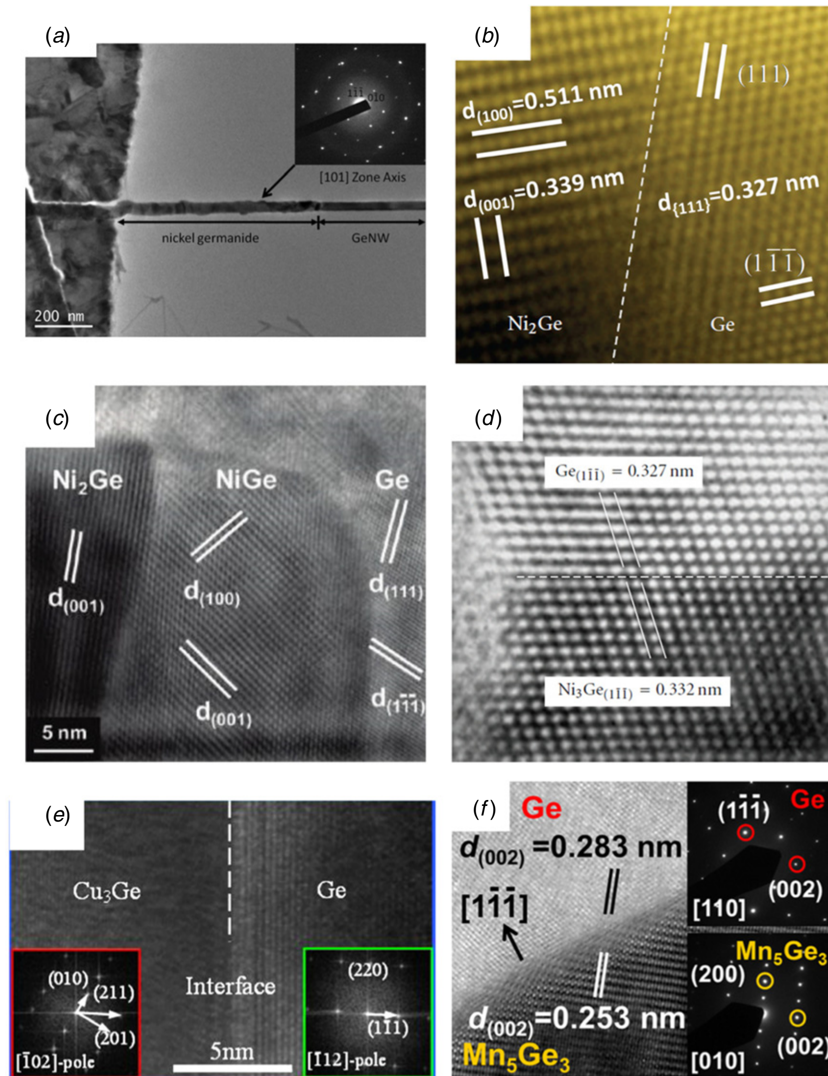

Figure 7. Different germanide/germanium interfaces from various reports. (Reproduced and adapted with permission): (*a*) $T = 400$ °C [46], (*b*) $T = 500$ °C, [49], (*c*) $T = 450$ °C, on Al_2O_3-coated NWs, [51], (*d*) $T = 650$ °C, [49], (*e*) $T = 300$ °C, [52], (*f*) $T = 450$ °C, [53].

NWs were not conformally covered by Al_2O_3. The significance of the short NiGe segment is the extracted negative hole SBH (−0.11 eV—no barrier) at the NiGe/Ge interface. VLS grown Ge NWs confined by Al_2O_3 were shown to have a mobility of 150–210 cm^2 (V s)$^{-1}$ after contact annealing.

Among the three common germanides interfacing with Ge, Ni_3Ge is the only one that has a similar crystal structure to Ge, and has a small lattice mismatch, 1.5%, as opposed to 56.3% for Ni_2Ge and 77% for NiGe. Tang *et al* noted that the large lattice mismatch in the case of NiGe and Ni_2Ge resulted in twisted growth modes where the epitaxial planes are not perpendicular to the NW axis ((1 1 1) direction). The closely lattice matched Ni_3Ge did not exhibit such 'twisted' growth mode, pertaining similar crystal orientation as the pristine Ge NW [49].

3.2. Other germanides

Besides Ni, several other metals have been investigated for germanide contacts to Ge NWs (table 6). Burchhart *et al* utilized copper contacts to form Cu_3Ge at 310 °C (figure 7(*e*)) [52]. Similar to the case of nickel germanide contacts, an atomically sharp interface between Ge and Cu_3Ge was observed, facilitating the creation of an ultra-short (15 nm) semiconducting channel. The crystallographic relationships between Ge and orthorhombic Cu_3Ge (a = 5.28 Å, b = 4.22 Å, c = 4.54 Å) were Ge($\bar{1}$ 1 2)//Cu_3Ge($\bar{1}$ 0 2) and Ge(1 $\bar{1}$ 1)//Cu_3Ge(2 1 1). An SBH of 218 meV was extracted from temperature-dependent current–voltage measurements. The same authors investigated Ti/Au as the drain/source contacts for NWFETs and reported very poor electrical conductivity [55]. This necessitated *ex situ* Ga^+ doping by focused ion beam implantation in order to reduce the effective SBH from 218 to 115 meV [56]. The extracted mobilities for Ge channels with Cu_3Ge contacts were 246 cm^2 (V s)$^{-1}$ for intrinsic Ge [52] and 142 cm^2 (V s)$^{-1}$ for Ga-doped channels [56]. For Ti/Au contacts, the non-implanted S/D regions exhibited Schottky-like behavior and much lower on-currents than the Ga-doped S/D regions for which a mobility of 148 cm^2 (V s)$^{-1}$ was estimated [55], without accounting for contact resistances [57].

In order to pave the way for Ge NWs for spintronic applications, it is critical to develop a high-Curie temperature

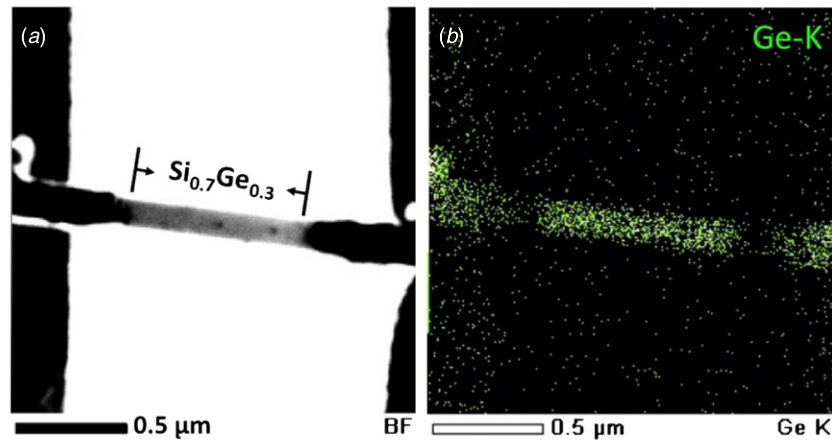

Figure 8. TEM and EDS map of a Ni-contacted $Si_{0.7}Ge_{0.3}$ alloy nanowire device annealed at 400 °C: (*a*) bright field TEM image and (*b*) Ge K signal showing Ge deficiency at the germano–silicide reaction front. Reproduced with permission from [60].

Table 6. Summary of interfacial phase of germanides formed by solid-state reaction between metal contacts and Ge NWs.

References	Interfacial phase	Reaction conditions	Lattice	*a* (Å)	*b* (Å)	*c* (Å)	Crystallographic relationship with Ge
[46]	Ni_3Ge_2	300–400 °C	Hexagonal	3.95	–	5.187	–
[48]	Ni_2Ge	400–500 °C	Orthorhombic	5.11	3.83	7.26	$Ge(0\ 1\ \bar{1})\ \Vert Ni_2Ge(0\ \bar{1}\ 1) Ge(1\ \bar{1}\ \bar{1}) \Vert\ Ni_2Ge(1\ 0\ 0)$
[49]	Ni_3Ge	650 °C	FCC	5.74	–	–	Same as Ge
[51]	NiGe	450 °C Al_2O_3 coated	Orthorhombic	5.38	3.42	5.81	$Ge(0\ 1\bar{1})\ \Vert NiGe(0\ 1\ 0) Ge(1\ \bar{1}\ \bar{1}) \Vert\ NiGe(0\ 0\ 1)$
[52]	Cu_3Ge	310 °C	Orthorhombic	5.28	4.22	4.54	$Ge(\bar{1}\ 1\ 2)//Cu_3Ge(\bar{1}\ 0\ 2)$ $Ge(1\ \bar{1}\ 1)//Cu_3Ge(2\ 1\ 1)$
[53]	Mn_5Ge_3	450 °C	Hexagonal	7.18		5.05	$Ge(1\ 1\ 0)//Mn_5Ge_3(0\ 1\ 0)$ $Ge(0\ 0\ 2)//Mn_5Ge_3(0\ 0\ 2)$

ferromagnetic contact with the conducting channel. Tang *et al* have investigated the formation of ferromagnetic germanide MnGe [53] and demonstrated electrical spin injection and detection in Ge-based NWFETs [58]. Hexagonal Mn_5Ge_3 ($a = 7.18$ Å, $c = 5.05$ Å) was formed at 450 °C (figure 7(*f*)). Its lattice mismatch to Ge of only 10.6% is significantly smaller than those of Mn–Si and Ni–Ge compounds. TEM diffraction patterns revealed the epitaxial relationships: $Ge(1\ 1\ 0)//Mn_5Ge_3(0\ 1\ 0)$ and $Ge(0\ 0\ 2)//Mn_5Ge_3(0\ 0\ 2)$. SB FETs with 0.25 eV SBH exhibited a channel hole mobility of 150–200 $cm^2\ (V\ s)^{-1}$, which is similar to previous results with NiGe contacts. The temperature-dependent resistance of a fully germanide Mn_5Ge_3 NW showed a clear transition behavior near the Curie temperature of Mn_5Ge_3 at about 300 K [53, 59].

3.3. Nano-channel contacts to GeSi Alloys and Ge/Si heterostructures.

Due to the complicated structure, little work has been reported on the propagation of Ni into alloyed GeSi and core/shell Ge/Si NWs. Jeon *et al* [60] showed that an atomically abrupt interface could be achieved between SiGe alloyed NWs and their germano-silicides with Ni or Ni/Au. For 100 nm diameter $Si_{0.7}Ge_{0.3}$ NWs annealed at 400 °C, the diffusion rate of Ni was found to be 16 nm s^{-1} while Ni/Au-mediated reaction occurs at a rate of 27 nm s^{-1}. The faster reaction rate of Ni/Au alloys was attributed to a smaller activation energy barrier for the diffusion of Au (1.12 eV) than that of Ni (1.9 eV) in Si [61]. The Au–Si and Au–Ge eutectic temperature is ~360 °C, and it is possible for Au–Si–Ge liquid phase to nucleate at a region of the NW when the Au concentration peaks above $\sim x_{Au} = 0.74$ in Ge [62] and $x_{Au} = 0.81$ in Si [63] at 400 °C, forming a low chemical potential region for additional Au accumulation. Ni would segregate out of the alloy upon cooling as demonstrated by Tang *et al* [64]. This Au-rich front was believed to be responsible for the resistive switching behavior of a Ni/Au contacted $Si_{0.95}Ge_{0.5}$ device which was absent in the case of Ni-only contacts, as expected from the lower hole barrier for a Au–Si contact (0.34 eV) [65] compared to that of NiSi contacts (table 5). One interesting observation in the solid-state reaction of alloyed SiGe NWs was the abrupt reduction of Ge concentration in the Ni (with or without Au) germano-silicide at the reaction front, while Ge was still present in the germano-silicide segment far from the reaction front. Shown in figure 8 are spatial maps of the Ni-contacted $Si_{0.7}Ge_{0.3}$ NW in bright field TEM and energy dispersive spectroscopy signal of the Ge-K line showing clear deficiency of Ge near the contact. It was interpreted that with NiSi having lower formation energy (-45 kJ mol^{-1}) than NiGe (-32 kJ mol^{-1}), Ni preferred to react with Si rather than with Ge [60]. In a NiGeSi compound, Pey *et al* [66] found that mobile Ge atoms can diffuse out of the NiGeSi front, which can also reduce the concentration of Ge. Additional theoretical investigations or *in situ* STEM experiments are likely to reveal the original cause of the Ge concentration reduction at the reaction front of a NiGeSi alloy.

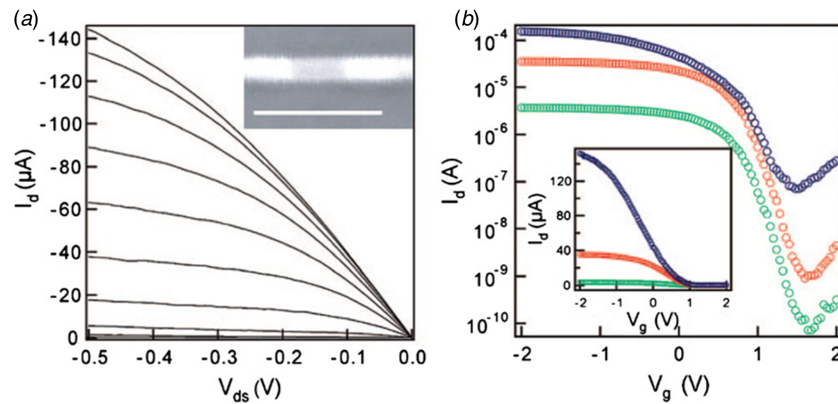

Figure 9. Electrical characteristics of a 40 nm channel length Ge/Si core/shell NWFET: (*a*) output I_d– V_{ds} with V_g varying from of −2 to 2 V in increments of 0.4 V and (*b*) transfer $I_d - V_g$ at $V_{ds} = -10$ mV (green circles), −100 mV (red circles) and −500 mV (blue circles). Inset in panel (*a*) illustrates the SEM image of the ultra-short channel length Ge/Si core/shell NW whose scale bar is 100 nm. Reproduced with permission from [67].

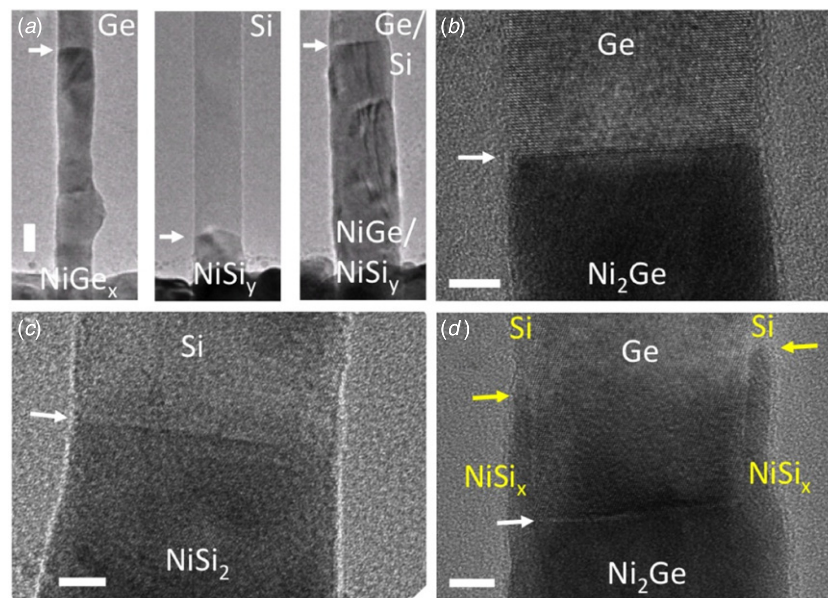

Figure 10. Solid-state reaction of Ni with (*a*) Ge, Si and Ge/Si core/shell NWs at the same annealing condition: 300 °C for 30 s under forming gas (5%:95% vol. H_2/N_2). Reaction is faster in Ge and Ge/Si NWs than that in Si. (*b*)–(*d*) High magnification TEM images of the (*b*) Ge-Ni_2Ge, (*c*) Si-$NiSi_2$, and (*d*) Ge/Si-$Ni_2Ge/NiSi_x$ core/shell NWs showing abrupt interfaces for the case of pure Ge and Si NWs, and two interfaces in the core/shell NW where the $NiSi_x$ reaction front leads the Ni_2Ge reaction front.

Another configuration of SiGe NWs is the Ge/Si core/shell heterostructure. Compared to homogeneous Ge, Si or SiGe NWs, Ge/Si core/shell structure possesses the capability of energy band-edge engineering due to the abrupt hetero-interface in radial directions [44]. The type-II band alignment between Ge and Si (the conduction and valence bands of Si lie below those of Ge) creates a hole accumulation in the Ge core and separates the confined carriers from the outer Si shell surface, in a process similar to conventional modulation doping, thus enhancing the hole mobility [68, 69]. Solid-state reaction between the nickel contacts and a Ge/Si core/shell NW enabled the first NWFETs with sub-100 nm channel length [67], and resulted in efficient electrostatic gate to channel coupling with excellent NWFET performance when compared to lithographically patterned source/drain contacts [70]. Figure 9 shows the output I_d–V_{ds} and transfer I_d–V_g curves of the shortest channel length (40 nm) NWFETs based on Ge/Si core/shell structure [67]. Devices made utilizing Ni solid-state reaction with Ge/Si core/shell NWs with 40 and 70 nm channel length were shown to outperform Si p-MOSFETs, and were believed to operate very close to the ballistic transport limit.

With the power of TEM, our work focused on revealing atomic scale details about the NiGe/NiSi–Ge/Si core/shell interfaces and controlling the compound reaction to further optimize device architecture and performance. Synthesis of epitaxial Ge/Si core/shell NWs without *ex situ* chemical or thermal treatments is described elsewhere [32, 71]. We found that the details of the Ni-Ge/Si NW interface played an important role in controlling the solid-state reaction of Ni with heterostructured Ge/Si NWs [72]. Unlike in homogeneous Ge or Si in either bulk or NW forms, where Ni reacts more easily with Ge than with Si, in Ge/Si core/shell NWs, Ni reacted first with the Si shell and led the reaction along the NW

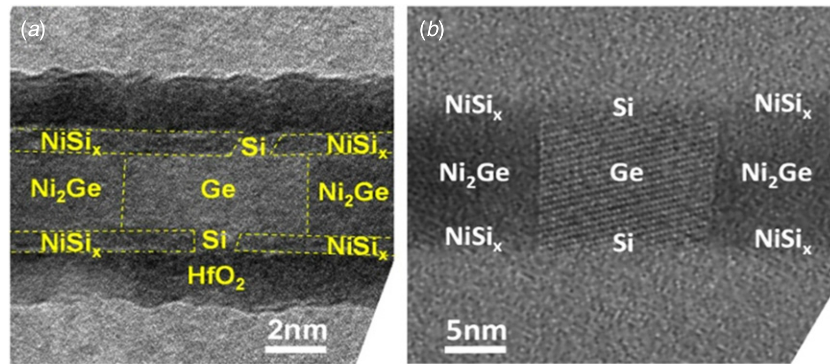

Figure 11. Toward ultra-short channel length in Ge/Si core/shell NW: (*a*) Ni pads in contact with Si facilitating a $NiSi_x$ shell front leading ahead from the Ni_2Ge front in the core. A metallic shell would short the channel before an ultra-short Ge channel is obtained. (*b*) Ni pads in direct contact with the Ge core (by selectively removing the Si shell underneath the Ni pads) allowing simultaneous propagation of both $NiSi_x$ and Ni_2Ge. An ultra-short Ge channel can be achieved without being shorted in the shell. Reproduced with permission from [72].

axis at a similar propagation rate as the lagging Ni_2Ge front (figure 10). Without proper management, this would hamper the realization of ultra-short channel length FETs from this core/shell structure, as the extended $NiSi_x$ shells from two sides can potentially merge and short the device before an ultra-short Ge channel can be attained. By selectively removing the Si shell underneath the Ni pads to promote early Ni_2Ge formation, simultaneous propagation of the Ni_2Ge and the $NiSi_x$ was accomplished (figure 11). This technique has been utilized to successfully demonstrate a 2 nm Ge/Si gap in the heterostructured NW [73].

On the electrical side, the effectiveness of the Si shell in Ge/Si core/shell NWs in enhancing the hole mobility has been demonstrated [69, 74]. The SBH has not been reported for the $Ni_2Ge/NiSi_x$ contact to Ge/Si core/shell NWs but we found that the contact resistance is negligible compared to channel resistance for ∼250–400 nm long NWFETs with the gate metal fully overlapped with source and drain germanides. For metal–compound contacts in NW devices, extraction of contact resistance with the 4-probe technique is inadequate as it can only measure the contact resistance between the metal/germanide interfaces, but not at the important germanide/semiconductor interface. Transmission line measurement is thus a more preferred method. We fabricated multiple Ni pads with variable spacings over a single NW to extract the contact resistance. The device was processed on a 50 nm thick SiN membrane so that the unreacted semiconductor NW segments can be precisely measured with TEM. As shown in figure 12, the contact resistance of the NWFET is below 10 kΩ, which is significantly smaller than typical resistance values of a NWFET device made on the same type of NWs and operating at maximum transconductance. This suggests that the contact resistance is negligible in our Ge/Si core/shell NWFET performance analysis and mobility extraction. The extracted hole mobility in our Ge/Si core/shell NWFETs was in the range of 150–200 cm^2 $(V\ s)^{-1}$ and was shown to be independent of the NW diameter. This result further validates the advantage of the core/shell architecture, which makes carriers immune from surface scattering effects at the Si/dielectric interfaces [74].

3.4. Performance of Ge and Ge/Si NWFETs with germanide contacts

As mentioned above, the motivation for Ge-based NWs is the enhanced mobility due to either intrinsically smaller hole effective mass or strain and bandgap engineering. Most of the works reviewed in this section reported both structural characterization of germanide/germanium interfaces with HRTEM and electrical properties of the junction with mobility extraction via FET performance. However, due to uncertainties of the dielectric constant, gate capacitance and contact resistance, the extraction procedure might not be consistent from one reference to another, and the mobility values cannot be directly compared. Moreover, back-gated configuration tends to result in higher mobility than top-gate geometry, with a possible explanation of modifying barrier heights/widths for hole injection with a back-gate or effectively the contact resistance. In order to provide a comprehensive assessment on the electrical characterization, we summarize in table 7 the main NWFET performance merits in the relationship with device dimensions and measurement conditions for nanoscale compound contacts to Ge and Ge/ Si core/shell NWFETs. It is important to note that Ge/Si core/shell NWs clearly exhibited superior mobility than homogeneous Ge devices in top-gate configuration and that the extracted mobility of top-gate Ge NWs is lower than that extracted from back-gate Ge NWs. Despite lower apparent mobility in top-gate configuration, the more efficient electro-static coupling between the gate voltage and the conduction channel leads to a generally higher transconductance, $g_m = \frac{dI_{DS}}{dV_{GS}}$, larger I_{max}/I_{min} ratio, as well as a steeper sub-threshold slope, $SS^{-1} = \left(\frac{d\log(I_{DS})}{dV_{GS}}\right)^{-1}$.

3.5. Asymmetric germanide–silicide SBFETs.

Our discussion thus far focused on SBFETs and NWFETs with symmetric alloyed contacts of either silicides to Si NWs or germanides to Ge NWs. It is possible however to realize Ge–Si heterostructures along the axis of a NW [33] thereby providing the opportunity for axial bandgap engineering along the charge carrier transport direction. This offers a unique opportunity for exploring nanochannel devices with asymmetric contacts to assist charge transport in one desired direction in on-state and

Table 7. Performance summary of Ge-based NWFETs with germanide contacts. SBH is the hole Schottky barrier height, SS^{-1} is the inverse sub-threshold slope.

References	Reaction temperature	Metal/ phases	SBH (eV)	Diameter (nm)	Channel length (μm)	$-V_d$(V)	SS^{-1} (V dec^{-1})	g_m(μS)	$\mu C = g_m L V^{-1}$ (μS μm V^{-1})	Gate dielectric	Mobility cm^2 $(V s)^{-1}$	I_{max}/ I_{min}	Note
[51]	450 °C/20 s	NiGe	−0.11	70	0.67	0.1	1.74 @ 20 mV	0.2	1.5	330 nm SiO_2	210	10^5	Backgate Al_2O_3 coated
[53]	450 °C	Mn_5Ge_3	0.25	50	0.5	0.1	3.81	0.25	1.3	330 nm SiO_2	170	10^5	Backgate Al_2O_3 coated
[48]	400 °C/15 s	Ni_2Ge	0.2	40	3	0.1	~5	0.013	0.4	330 nm SiO_2	65	10^3	Backgate SFLS grown
[56]	300 °C	Cu_3Ge	0.218	250	–	–	0.83	–	3.7	20 nm SiO_x	142	10^3	Backgate Ga-doped channel
[68]	300 °C/15 s	$NiGe_x/NiSi_y$	–	18	190	0.01	0.105	3	57	4 nm HfO_2	730 @10 mV; 142 @ 1V	$>10^5$	Top gate Core/shell
[67]	300 °C	$NiGe_x/NiSi_y$	–	18	40	0.5	~0.19	91	7.3	4 nm HfO_2	91	10^5	Top gate Core/shell
[67]	300 °C	$NiGe_x/NiSi_y$	–	18	70	0.5	~0.2	78	10.9	4 nm HfO_2	136	10^5	Top gate Core/shell
[74]	300 °C/30 s	Ni_2Ge	–	30	400	0.1	0.26	1.1	4.5	10 nm HfO_2	50	10^5	Top gate Ge NW
[74]	300 °C/30 s	$Ni_2Ge/NiSi_y$	–	20	300	0.1	0.14	4	12	10 nm HfO_2	200	10^6	Top gate Core/shell

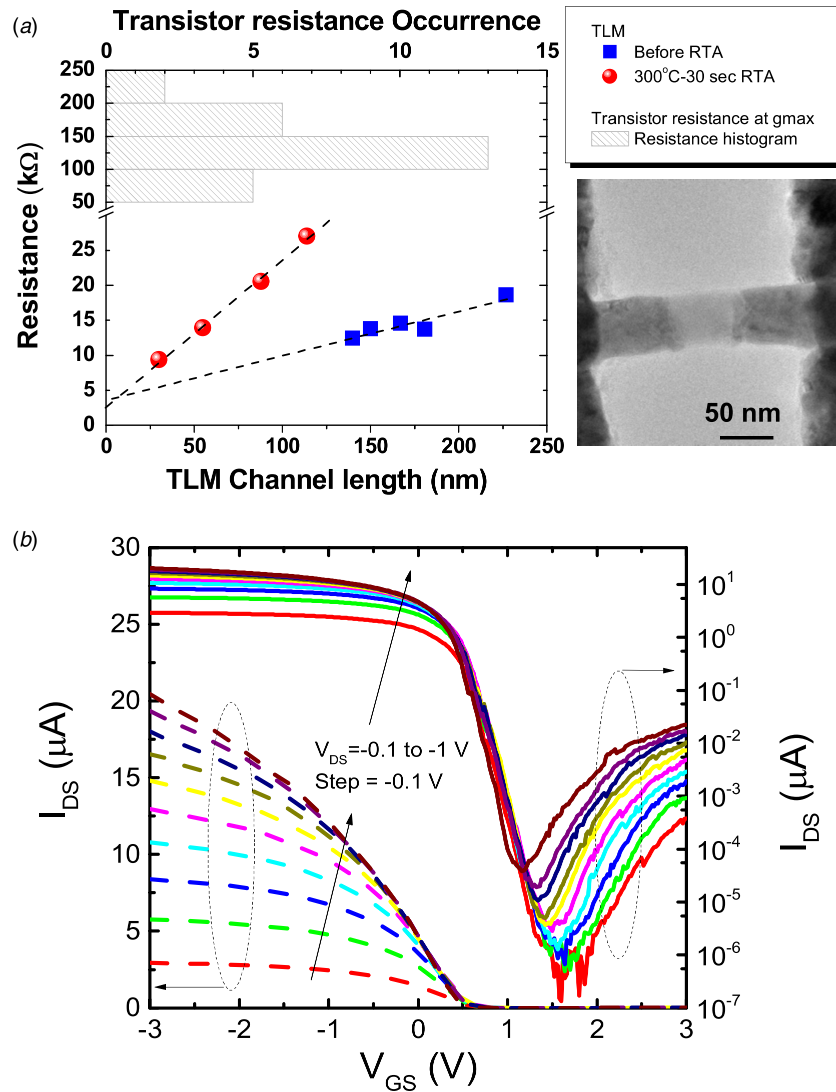

Figure 12. (*a*) NW resistance as a function of un-reacted semiconductor channel lengths. The contact resistance in Ge/Si core/shell NWs is extracted to be below 10 kΩ, which is much smaller than the typical resistance of the NW FET operating at maximum transconductance (histogram peaks at 100–150 kΩ). (*b*) Bias-dependent transfer characteristics of a typical Ge/Si core/shell NWFET with 378 nm channel length and 17.1 nm diameter. Reproduced with permission from [74].

block it in the opposite one in off-state. In such a device, the difference in barrier heights at either end of the channel can add to the total potential drop in the channel and enhance current transport of thermionically emitted carriers of the source SB. This configuration is illustrated in figure 13(*a*)), where a Si–Ge axial NW heterostructure used for Silvaco-Atlas simulations is shown together with the energy band-edge diagram along the channel length in on-state condition. The potential drop across the valence band-edge along the channel can be expressed as [75]:

$$\left|E_{v(S)} - E_{v(D)}\right|/q = V_{SD} + \Delta E_{v(\text{Ge--Si})}/q + \varphi_{Bp(S)} - \varphi_{Bp(D)} \tag{10}$$

where V_{SD} is the applied source–drain voltage, $\Delta E_{v(\text{Ge–Si})}$~0.57 eV is the valence band offset between Ge and Si, $\varphi_{Bp(S)}$ is the hole SBH at the source side of the channel, and $\varphi_{Bp(D)}$ is the hole SBH at the drain side of the channel. The right-hand terms in equation (10) except of V_{SD} can be as large as 0.82 V for Ni silicide and germanide contacts to the Si and Ge portions of the NW, respectively, and is manifested as an additional potential drop that accelerate holes from the Si side to the Ge side of the channel. For a pure Si channel (dashed lines for the energy band-edge diagram in figure 13(*a*)), the larger hole SBH for Si compared to Ge near the drain imposes a negative slope of the valence band-edge near the drain which in turn leads to a backward field that opposes hole transport toward the drain and reduces I_{on} compared to the heterostructured one. Devices with Ni (figure 13(*b*)) or Ni silicide and germanide contacts made on axial Ge–Si heterostructure NWs showed excellent I_{SD} modulation with 10^7 I_{max}/I_{min} exceeding that of NWFETs made on pure p^+Ge or pure Si segments [75]. This device architecture adds an important ability to accommodate band-offsets and built-in electric fields in the conduction or valence bands, separately at the source or drain sides of SBFETs, by proper selection of metal–semiconductor barrier heights with the

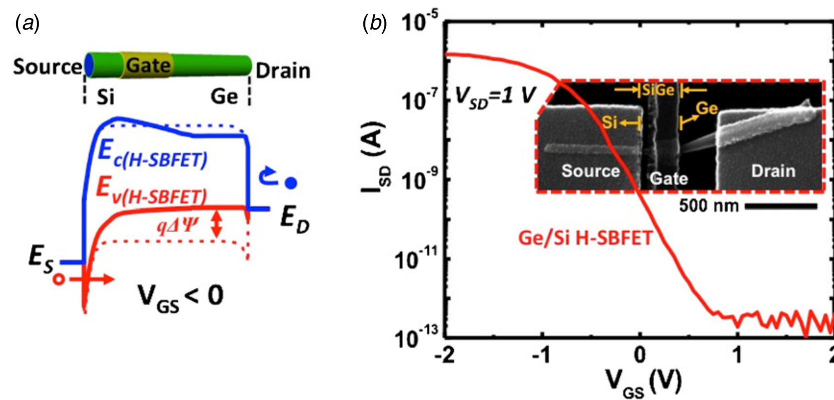

Figure 13. (*a*) Simulated axial Ge–Si heterostructures SBFET device schematic and energy band-edge diagrams, extracted at the axis of the NW channel in on-state. Dashed lines correspond to the situation of a pure Si channel under the same bias conditions. (*b*) Transfer curve of a p^+ Ge–Si NW heterostructure SBFET showing 10^7 I_{on}/I_{off} ratio. Inset is an SEM image of the device with a source–gate spacing of ∼40 nm, gate length of ∼200 nm, and gate–drain spacing is ∼260 nm (V_{SD} = 1 V). Reproduced with permission from [75].

metal contacts thus expanding the available range of advanced architectures for next generation semiconductor devices.

4. Conclusion

The atomic level understanding of Ni compound and alloy contact formation to nanoscale channels by solid-state diffusion sets new frontiers to control and tailor the contact structure, morphology, and electronic properties. While several technologies such as photovoltaics and integrated circuits are at the horizons of deciding on prospective high performance and cost effective materials, continual growth in understanding nanoscale contact formation and optimization is urgently desired to co-develop and advance. It is our hope that this paper provides a timely and fair account to the current understanding of state of the art contact technology to Si, Ge and their heterostructured nanoscale channels and the remaining issues that require further development in the foreseeable future.

Acknowledgments

The authors are grateful to numerous discussions and contributions of several colleagues including Professors King-Ning Tu, S S Lau, S T Picraux, Edward T Yu and to the contributions of Drs Yang Liu and Xiaohua Liu. The authors are also grateful for the support of staff members at the Integrated Laboratory at the Center for Integrated Nanotechnologies at Sandia National Laboratories and Los Alamos National Laboratory, and the staff members at the nano3 facilities at the Qulacomm Institute at the University of California, San Diego. This work was performed, in part, at the Center for Integrated Nanotechnologies, an Office of Science User Facility operated for the US Department of Energy (DOE) Office of Science. Los Alamos National Laboratory, an affirmative action equal opportunity employer, is operated by Los Alamos National Security, LLC, for the National Nuclear Security Administration of the US Department of Energy under contract no. DE-AC52–06NA25396 and was supported by Laboratory Directed Research and Development (LDRD) funds and a faculty start-up fund at UC, San Diego.

References

[1] Chen L J 2004 *Silicide Technology for Integrated Circuits* (London: Institution of Electrical Engineers)
[2] Christian L, Francois M d'H and Shi-Li Z 2007 *Silicides, in Handbook of Semiconductor Manufacturing Technology* 2nd edn (Boca Roton, FL: CRC Press) pp 10–52
[3] Kuhn K J 2012 Considerations for ultimate CMOS Scaling *IEEE Trans. Electron Devices* **59** 1813–28
[4] Tu K N *et al* 1974 Epitaxial-growth of nickel silicide $NiSi_2$ on silicon *Japan. J. Appl. Phys.* **2** 669–72
[5] Tang W *et al* 2102 Ultrashort channel silicon nanowire transistors with nickel silicide source/drain contacts *Nano Lett.* **12** 5893–9793
[6] Lin Y C *et al* 2010 Growth of nickel silicides in Si and Si/SiO*x* core/shell nanowires *Nano Lett.* **10** 4721–6
[7] Chen Y *et al* 2012 Kinetic competition model and size-dependent phase selection in 1D nanostructures *Nano Lett.* **12** 3115–20
[8] Chen Y *et al* 2013 Kinetic manipulation of silicide phase formation in Si nanowire templates *Nano Lett.* **13** 3703–8
[9] Lu K C *et al* 2007 *In situ* control of atomic-scale Si layer with huge strain in the nanoheterostructure NiSi/Si/NiSi through point contact reaction *Nano Lett.* **7** 2389–94
[10] Chou Y-C *et al* 2009 Homogeneous nucleation of epitaxial CoSi2 and NiSi in Si nanowires *Nano Lett.* **9** 2337–42
[11] Dellas N S *et al* 2009 Orientation dependence of nickel silicide formation in contacts to silicon nanowires *J. Appl. Phys.* **105** 094309
[12] Toman K 1952 The structure of Ni_2Si *Acta Crystallogr.* **5** 329–31
[13] Ogata K *et al* 2011 Ni-silicide growth kinetics in Si and Si/SiO_2 core/shell nanowires *Nanotechnology* **22** 365305
[14] Schlesinger M E 1990 Thermodynamics of solid transition-metal silicides *Chem. Rev.* **90** 607–28
[15] Pretorius R 1996 Prediction of silicide formation and stability using heats of formation *Thin Solid Films* **290–291** 477–84
[16] Hesse D *et al* 1993 Interfacial reaction barriers during thin-film solid-state reactions: the crystallographic origin of kinetic barriers at the NiS_2/Si(1 1 1) interface *Appl. Phys.* A **57** 415–25
[17] Teodorescu V *et al* 2001 *In situ* transmission electron microscopy study of Ni silicide phases formed on (0 0 1) Si active lines *J. Appl. Phys.* **90** 167–74
[18] d'Heurle F M 1988 Nucleation of a new phase from the interaction of two adjacent phases: some silicides *J. Mater. Res.* **3** 167–95

[19] Coia C 2009 Microstructure and growth kinetics of nickel silicide ultra-thin films synthesized by solid-state reactions *PhD Thesis* Ecole Polytechnique (Montreal, Canada) p 317

[20] Walser R M and Bene R W 1976 First phase nucleation in silicon–transition-metal planar interfaces *Appl. Phys. Lett.* **28** 624–5

[21] d'Heurle F M and Gas P 1986 Kinetics of formation of silicides: a review *J. Mater. Res.* **1** 205–21

[22] Appenzeller J *et al* 2006 Dual-gate silicon nanowire transistors with nickel silicide contacts *IEDM'06: Proc. Int. Electron Devices Meeting (San Francisco, CA)* pp 1–4

[23] Dellas N S *et al* 2011 Kinetics of reactions of Ni contact pads with Si nanowires *J. Mater. Res.* **26** 2282–5

[24] Gas P and d'Heurle F M 1998 *4 Diffusion in silicides, in Diffusion in Semiconductors* ed D L Beke (Berlin: Springer) pp 1–38

[25] Beregovsky M *et al* 2013 Diffusion formation of nickel silicide contacts in SiNWs *Solid-State Electron.* **80** 110–7

[26] Bracht H and Stolwijk N A 1998 *2 Diffusion in Si* ed D L Beke (Berlin: Springer) pp 12–134

[27] Tu K N, Chu W K and Mayer J W 1975 Structure and growth kinetics of Ni_2si on silicon *Thin Solid Films* **25** 403–13

[28] Katsman A *et al* 2010 Surface diffusion controlled formation of nickel silicides in silicon nanowires *J. Electron. Mater.* **39** 365–70

[29] Ciccariello J C, Poize S and Gas P 1990 Lattice and grain boundary self-diffusion in Ni_2Si: comparison with thin-film formation *J. Appl. Phys.* **67** 3315–22

[30] Yaish Y E *et al* 2011 Kinetics of nickel silicide growth in silicon nanowires: from linear to square root growth *J. Appl. Phys.* **109** 094303

[31] Kwan-Yong L *et al* 2010 Novel stress-memorization-technology (SMT) for high electron mobility enhancement of gate last high-k/metal gate devices *IEDM'10: Proc. IEEE Int. Electron Devices Meeting (San Francisco, CA)* pp 1–10

[32] Dayeh S A, Gin A V and Picraux S T 2011 Advanced core/multishell germanium/silicon nanowire heterostructures: morphology and transport *Appl. Phys. Lett.* **98** 163112

[33] Tang W *et al* 2013 Nucleation and atomic layer reaction in nickel silicide for defect-engineered Si nanochannels *Nano Lett.* **13** 2748–53

[34] Sze S M and Ng K K 2006 *Metal-Semiconductor Contacts, in Physics of Semiconductor Devices* (New York: Wiley) pp 134–96

[35] Maszara W P 2005 Fully silicided metal gates for high-performance CMOS technology: a review *J. Electrochem. Soc.* **152** G550–5

[36] Taur Y and Ning T H 2009 *Fundamentals of Modern VLSI Devices* vol 23 2nd edn (Cambridge: Cambridge University Press) p 656

[37] Tung R T 1984 Schottky-barrier formation at single-crystal metal–semiconductor interfaces *Phys. Rev. Lett.* **52** 461–4

[38] Tan E J *et al* 2008 Demonstration of Schottky barrier NMOS transistors with erbium silicided source/drain and silicon nanowire channel *IEEE Electron Device Lett.* **29** 1167–70

[39] Lin Y C *et al* 2008 Single crystalline PtSi nanowires, PtSi/Si/PtSi nanowire heterostructures and nanodevices *Nano Lett.* **8** 913–8

[40] Mongillo M *et al* 2011 Joule-assisted silicidation for short-channel silicon nanowire devices *ACS Nano* **5** 7117–23

[41] Wu W W *et al* 2010 Controlled large strain of Ni silicide/Si/Ni silicide nanowire heterostructures and their electron transport properties *Appl. Phys. Lett.* **97** 203110

[42] Wang D and Dai H 2002 Low-temperature synthesis of single-crystal germanium nanowires by chemical vapor deposition *Angew. Chem. Int. Edn Engl.* **41** 4783–6

[43] Lew K K *et al* 2003 Vapor–liquid–solid growth of silicon–germanium nanowires *Adv. Mater.* **15** 2073–6

[44] Lauhon L J *et al* 2002 Epitaxial core-shell and core-multishell nanowire heterostructures *Nature* **420** 57–61

[45] Takizawa H, Uheda K and Endo T 2000 NiGe2: a new intermetallic compound synthesized under high-pressure *J. Alloys Compd.* **305** 306–10

[46] Dellas N S *et al* 2010 Formation of nickel germanide contacts to Ge nanowires *Appl. Phys. Lett.* **97** 263116

[47] Dellas N S *et al* 2009 Orientation dependence of nickel silicide formation in contacts to silicon nanowires *J. Appl. Phys.* **105** 094309

[48] Tang J *et al* 2010 Single-crystalline $Ni_2Ge/Ge/Ni_2Ge$ nanowire heterostructure transistors *Nanotechnology* **21** 505704

[49] Tang J *et al* 2011 Formation and device application of Ge nanowire heterostructures via rapid thermal annealing *Adv. Mater. Sci. Eng.* **2011** 316513

[50] Izumi T *et al* 2004 Ferromagnetic properties of cyclically deformed Fe_3Ge and Ni_3Ge *Phil. Mag.* **84** 3883–95

[51] Tang J *et al* 2011 Oxide-confined formation of germanium nanowire heterostructures for high-performance transistors *ACS Nano* **5** 6008–15

[52] Burchhart T *et al* 2009 Atomic scale alignment of copper-germanide contacts for Ge nanowire metal oxide field effect transistors *Nano Lett.* **9** 3739–42

[53] Tang J *et al* 2012 Ferromagnetic germanide in Ge nanowire transistors for spintronics application *ACS Nano* **6** 5710–7

[54] Lin Y-C *et al* 2010 Growth of nickel silicides in Si and Si/SiO*x* core/shell nanowires *Nano Lett.* **10** 4721–6

[55] Burchhart T *et al* 2011 Tuning the electrical performance of Ge nanowire MOSFETs by focused ion beam implantation *Nanotechnology* **22** 035201

[56] Burchhart T *et al* 2010 High performance Ω-gated Ge nanowire MOSFET with quasi-metallic source/drain contacts *Nanotechnology* **21** 435704

[57] Dayeh S A *et al* 2007 High electron mobility InAs nanowire field-effect transistors *Small* **3** 326–32

[58] Tang J *et al* 2013 Electrical spin injection and detection in $Mn_5Ge_3/Ge/Mn_5Ge_3$ nanowire transistors *Nano Lett.* **13** 4036–43

[59] Tang J *et al* 2012 Electrical probing of magnetic phase transition and domain wall motion in single-crystalline Mn_5Ge_3 nanowire *Nano Lett.* **12** 6372–9

[60] Jeon E-K *et al* 2009 Resolving microscopic interfaces in $Si_{1-x}Ge_x$ alloy nanowire devices *Nanotechnology* **20** 115708

[61] Kanno H *et al* 2005 Low-temperature formation of Poly-$Si_{1-x}Ge_x$ (x: 0–1) on SiO_2 by Au-mediated lateral crystallization *Japan. J. Appl. Phys.* **44** 2405

[62] Okamoto H and Massalski T B 1984 The Au–Ge (Gold–Germanium) system *Bull. Alloy Phase Diagr.* **5** 601–10

[63] Okamoto H and Massalski T B 1983 The Au–Si (Gold–Silicon) system *Bull. Alloy Phase Diagr.* **4** 190–8

[64] Tang W *et al* 2013 Gold catalyzed nickel disilicide formation: a new solid–liquid–solid phase growth mechanism *Nano Lett.* **13** 6009–15

[65] Sze S M 1981 *Physics of Semiconductor Devices* (New York: Wiley)

[66] Pey K L *et al* 2002 Thermal reaction of nickel and $Si_{0.75}Ge_{0.25}$ alloy *J. Vac. Sci. Technol.* A **20** 1903–10

[67] Hu Y *et al* 2008 Sub-100 nanometer channel length Ge/Si nanowire transistors with potential for 2 THz switching speed *Nano Lett.* **8** 925–30

[68] Xiang J *et al* 2006 Ge/Si nanowire heterostructures as high-performance field-effect transistors *Nature* **441** 489–93

[69] Nah J *et al* 2011 Role of confinement on carrier transport in Ge–Si_xGe_{1-x} Core–shell nanowires *Nano Lett.* **12** 108–12

[70] Jing G *et al* 2003 Electrostatics of nanowire transistors *Nanotechnol. IEEE Trans.* **2** 329–34

[71] Dayeh S A *et al* 2012 Direct measurement of coherency limits for strain relaxation in heteroepitaxial core/shell nanowires *Nano Lett.* **13** 1869–76

[72] Dayeh S *et al* 2013 (Invited) nanoscale heterogeneous reactions and interfaces in Ge/Si and for III–V on Si integrated devices *ECS Trans.* **58** 115–25

[73] Nguyen B-M, Liu Y and Dayeh S 2013 unpublished

[74] Nguyen B-M *et al* 2014 Diameter-independent hole mobility in Ge/Si core/shell nanowire field effect transistors *Nano Lett.* **14** 585–91

[75] Dayeh S A, Dickerson R M and Picraux S T 2011 Axial bandgap engineering in germanium–silicon heterostructured nanowires *Appl. Phys. Lett.* **99** 113105